Supporting Information

A high-pressure enabled high-entropy $(CrFeCoNiMn)_4S_5$ composite anode for durability and high-rate sodium-ion batteries

Jiahui Wang[a], Qiaoyu Liu[b,c], Donghan Jia[b], Kefeng Liu[b], Zhenning Gao[a], Chaoxian Wu[a], Qingao Zhao[b,d], Lailei Wu[e], Jian Zhang[d], Xin Zhang[a]*, Gongkai Wang[a]*, Huiyang Gou[b]*,

[a] "The Belt and Road Initiative" Advanced Materials International Joint Research Center of Hebei Province, School of Material Science and Engineering, Hebei University of Technology, Tianjin, 300130, China

[b] Center for High Pressure Science & Technology Advanced Research, Beijing 100193, China

[c] College of Materials Science and Engineering, Yanshan University, Qinhuangdao 066004, China

[d] State Key Laboratory of Crystal Materials and Institute of Crystal Materials, Shandong University, Jinan 250100, China

[e] College of Material Science and Engineering, Liaoning Technical University, Fuxin123000, China

***Corresponding authors**:

zhang_xin@hebut.edu.cn; wang.gongkai@hebut.edu.cn; huiyang.gou@hpstar.ac.cn

Experimental Section:

Materials Synthesis: Synthesis of HES@CNOs, CFNS@CNOs, and CS@CNOs: All chemicals, including chromium, iron, cobalt, nickel, manganese, and sulfur powders, were purchased from Macklin and used as received without further purification. The purity of all reagents exceeded 99.99%. Cr_4S_5 (CS), $[CrFeNi]_4S_5$ (CFNS), and $[CrFeCoNiMn]_4S_5$ (HES) were synthesized using a high-pressure and high-temperature (HPHT) Cubic Press (GY 420). Detailed schematics of the pyrophyllite blocks utilized for synthesizing the samples are provided in the supplementary materials. Initially, metal powders and sulfur were mixed in a molar ratio of 4:5 and ground in an agate mortar for over 30 minutes. The mixed powder was then placed in a mold and pre-pressed into a cylindrical block (diameter: 5 mm; height: 3 mm) under a pressure of 20 MPa before being transferred to a h-BN capsule. The assembled sample underwent isothermal annealing at 1200 °C under 5 GPa for 40 minutes, followed by gradual cooling to 1100 °C over 40 minutes. After cooling, the product was extracted from the assembly and washed multiple times with ethanol. The desired material was obtained by further refining the sintered samples with carbon nano onions (CNOs) through high-energy mechanical milling (HEMM) using a SPEX 8000D mill. This process involved a ball-to-powder ratio of 20:1, operating at a speed of 1725 rpm for 10 hours under an argon atmosphere.

Materials Characterizations: Powder X-ray diffraction (PXRD) was conducted using a Bruker D8 Discover diffractometer, employing Cu-Kα radiation at a test voltage of 40 kV and a scanning rate of 0.24° min^{-1}. The single crystal CIF data obtained from the analysis were refined using Fullprof software to provide a detailed examination of the crystal structure. Raman spectra were acquired with a confocal micro-Raman spectrometer (LabRam HR Evolution, Horiba), utilizing a 532 nm laser as the excitation source. X-ray photoelectron spectroscopy (XPS, Thermo Scientific, ESCALAB 250), using Al-Kα radiation, was employed to investigate surface chemical valence states and elemental composition. Nitrogen adsorption-desorption isotherms were recorded and analyzed using the SSA-7000 analyzer at liquid nitrogen temperature. The microscopic morphology and structure were characterized through field emission scanning electron microscopy (FESEM, JEOL 7900 F), transmission electron microscopy (TEM, Tecnai LaB6), and energy dispersive spectroscopy (EDS).

Electrochemical Measurements: For half-cells, working electrodes were prepared

by mixing the active material, Super-P, and polyvinylidene fluoride (PVDF) in N-methyl pyrrolidone (NMP) at a weight ratio of 7:1.5:1.5. The resulting slurry was uniformly applied onto copper foil and carbon-coated aluminum foil, then dried at 75 °C for 12 hours. The mass loading of the electrodes was maintained at 0.7–1.0 mg cm^{-2}, with each working electrode having a diameter of 10 mm. CR 2025 button cells were assembled in an argon-filled glove box (H_2O < 0.01 ppm, O_2 < 0.01 ppm). Sodium foil served as the counter electrode, while Celgard 2400 and glass microfibers (GF/D) were used as separators. The electrolyte consisted of 1.0 M $NaPF_6$ mixed in dimethyl ether (DME). The electrochemical performance of the cells was evaluated using a battery testing system (Neware BTS4000), with voltage windows set at 0.01–3 V and 0.3–3 V. For the full-cell cathode electrode, $Na_3V_2(PO_4)_3$ (NVP) (80 wt%), carbon black (10 wt%), and PVDF (10 wt%) dissolved in NMP were mixed to form a slurry, which was then coated onto aluminum foils. The anode was pre-treated at a current density of 0.5 A g^{-1} for three cycles in the half-cell before being disassembled and reassembled with the cathode. The voltage windows for the full-cell tests were set at 0.6–3.8 V and 0.6–3.4 V. Cyclic voltammetry (CV) and electrochemical impedance spectroscopy (EIS) measurements (100 kHz–0.01 Hz) were performed using an AMETEK Princeton Versa STAT electrochemical workstation.

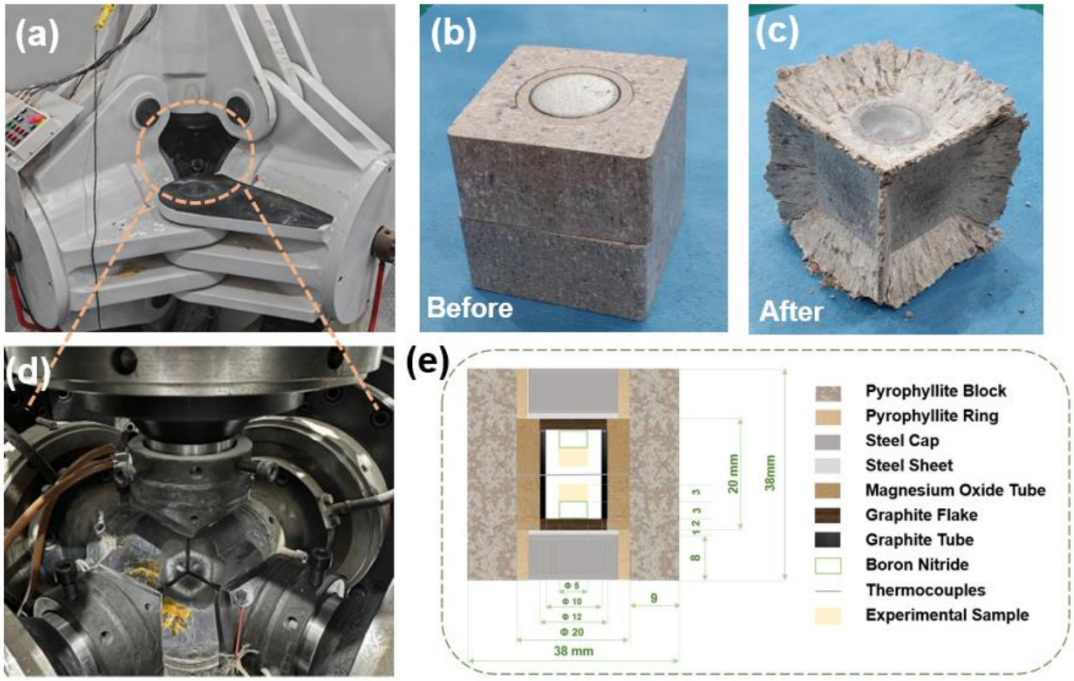

Fig. S1 (a) Cubic Press. (b,c) Assembled pyrophyllite block before and after pressure.

(d) The inner cavity of the Cubic Press. (e) Schematic diagrams of the assembled pyrophyllite block.

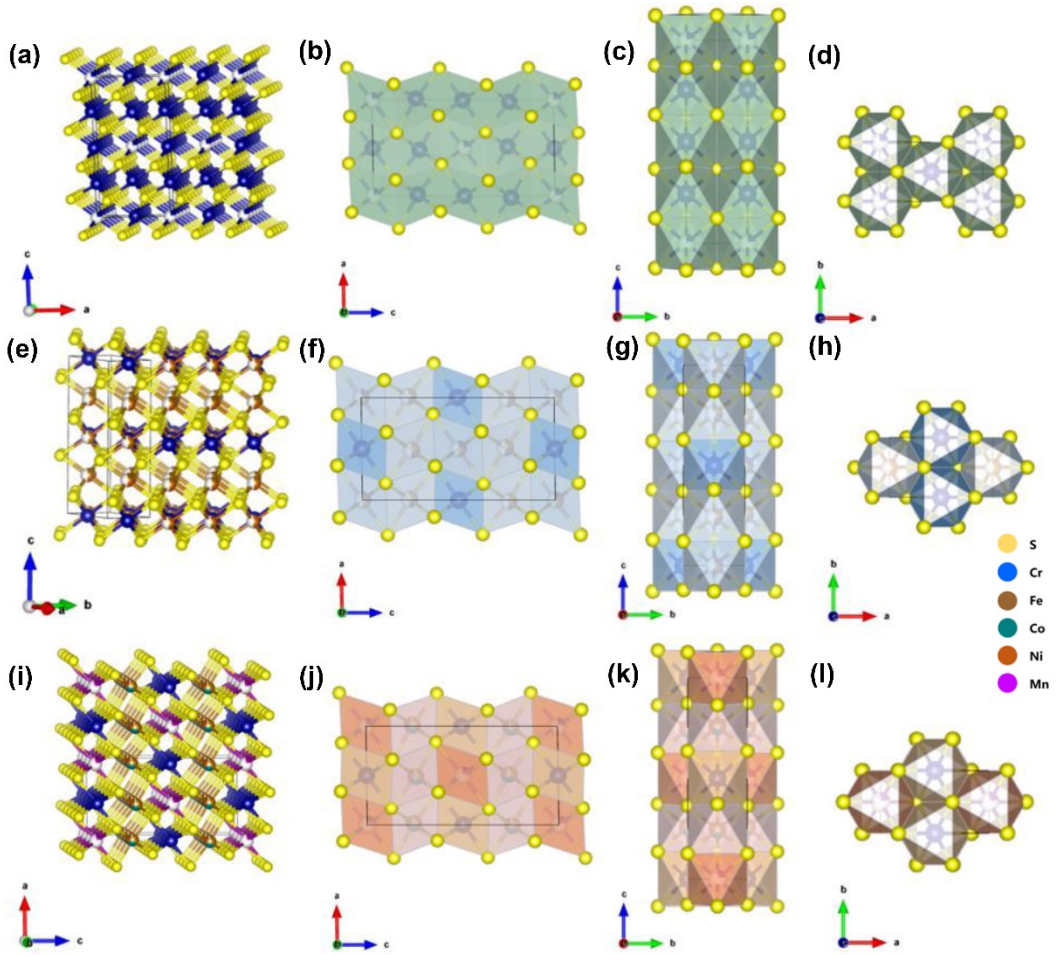

Fig. S2 The crystallographic information files of (a-d) CS, (e-h) CFNS, and (i-l) HES.

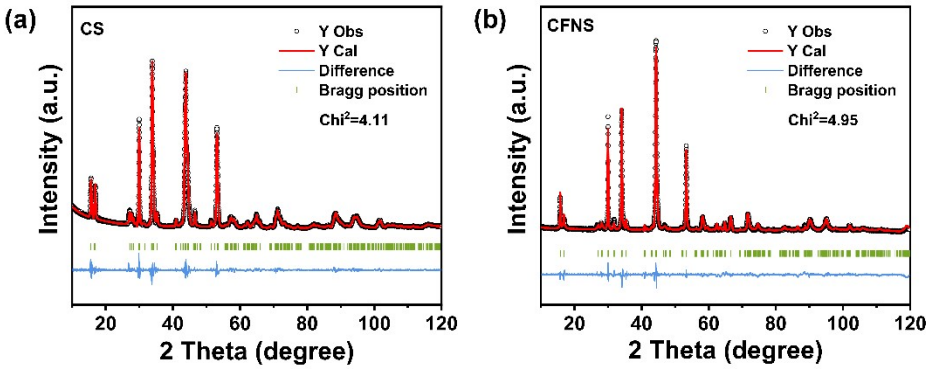

Fig. S3 Rietveld refinement of the powder XRD pattern of (a) CS, and (b) CFNS.

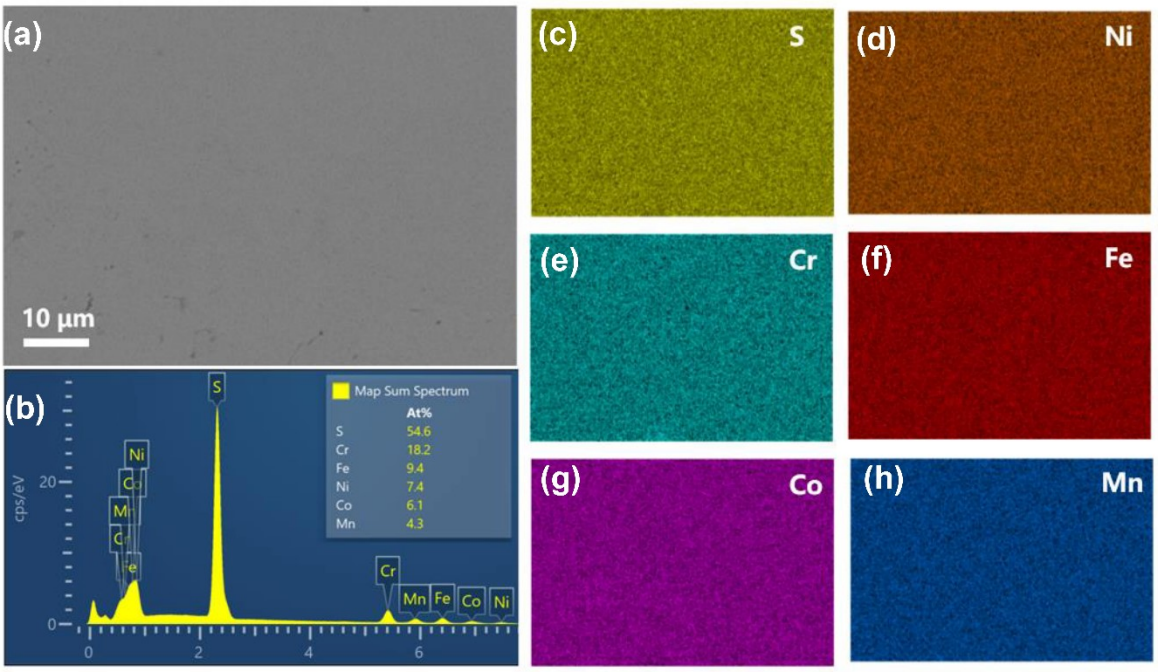

Fig. S4 SEM morphology characterizations of HES. (a) BSE image. (b) Statistics of backscattered electron components of HES. (c-h) EDS mapping.

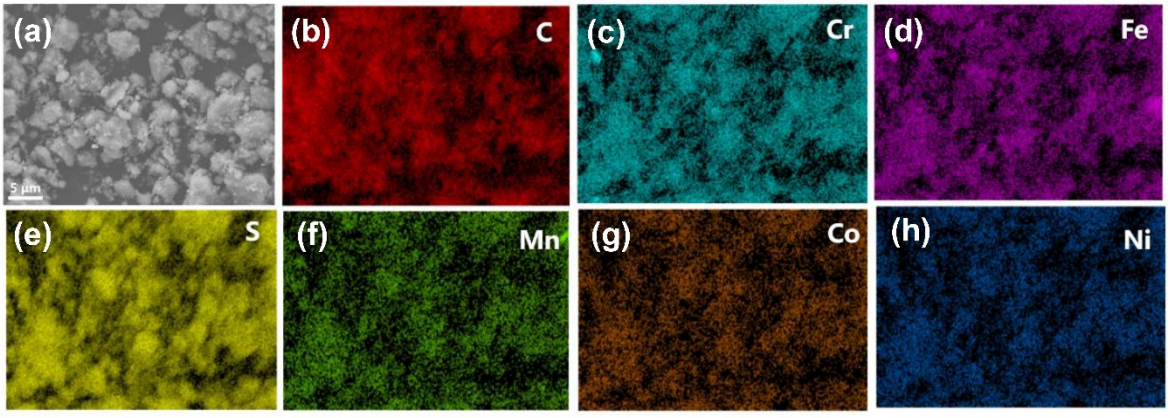

Fig. S5 Morphology characterizations. SEM images of (a) HES@CNOs, (b-h) EDS mapping.

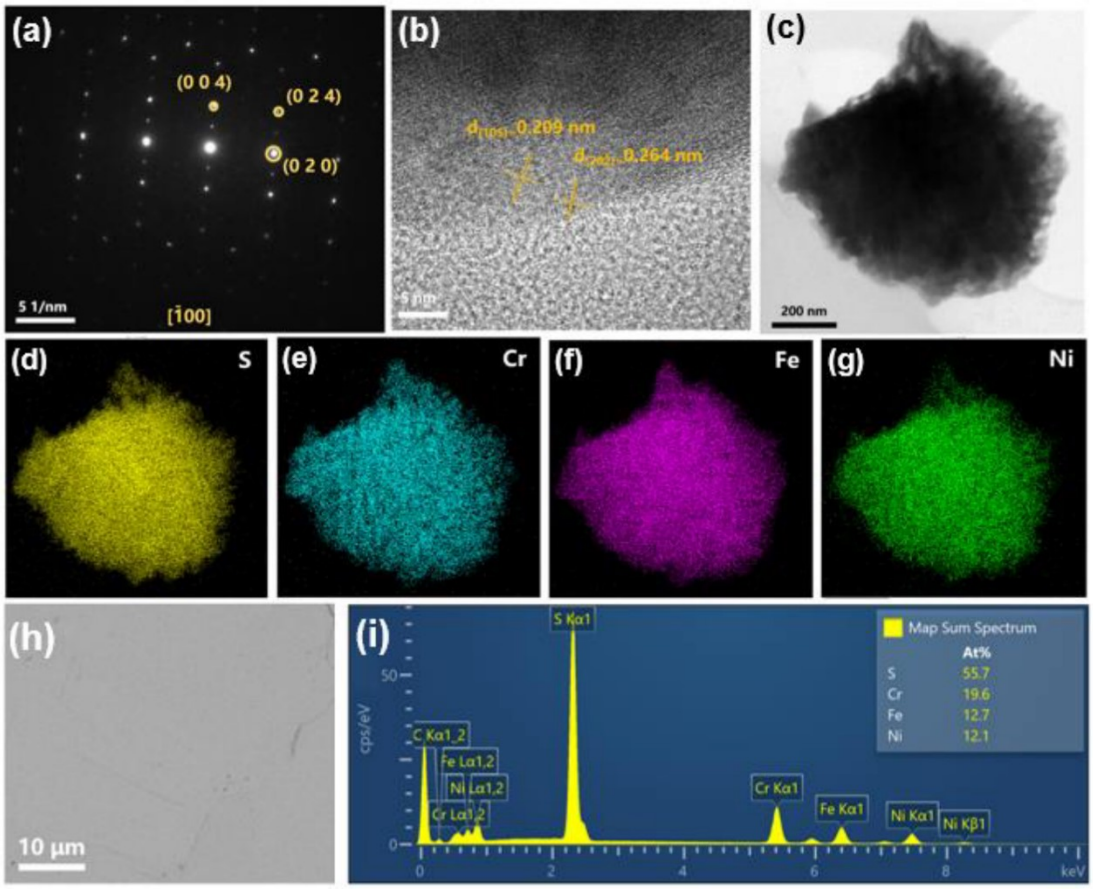

Fig. S6 (a) SAED pattern, (b) HRTEM, (c) TEM images of CFNS. (d-g) EDS mapping. (h) BSE image. (i) Statistics of backscattered electron components of CFNS.

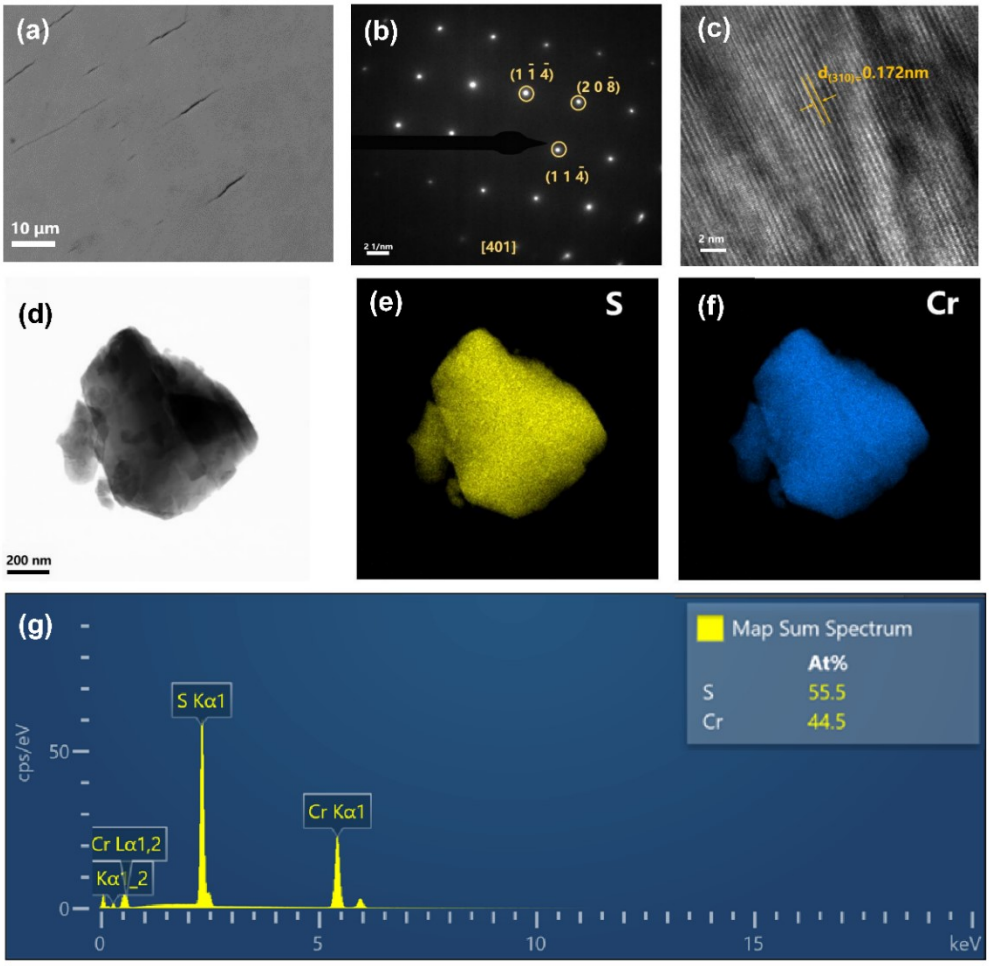

Fig. S7 (a) BSE image, (b) SAED pattern, (c) HRTEM, (d) TEM images of CS. (e,f) EDS mapping. (g) Statistics of backscattered electron components of CS.

Furthermore, the SAED pattern (Fig. S6a) identified the (020), (004), and (024) planes of CFNS. The HRTEM image in Fig. S6b indicated lattice spacings of 0.209 nm and 0.264 nm corresponding to the (105) and (202) planes, respectively. EDS analysis further confirmed the uniform distribution of Fe, Cr, Ni, and S within CFNS, as illustrated in Fig. S6d-g. Fig. S6h and S7a present BSE images for CFNS and CS. The ratio of metal elements (M = Cr, Fe, Ni) to sulfur (S) was determined to be 4:5, as shown in Fig. S5i and S6g. The SAED pattern displayed distinct single-crystal diffraction signals from the $(1\bar{1}\bar{4})$, $(20\bar{8})$, $(11\bar{4})$ planes of monoclinic CS. Additionally, clear lattice fringes associated with CS were observed on the (310) crystal plane in Fig. S7c, with an interplanar spacing measured at 0.172 nm. EDS analysis further indicated a uniform distribution of elements within CS (Fig. S6d-f).

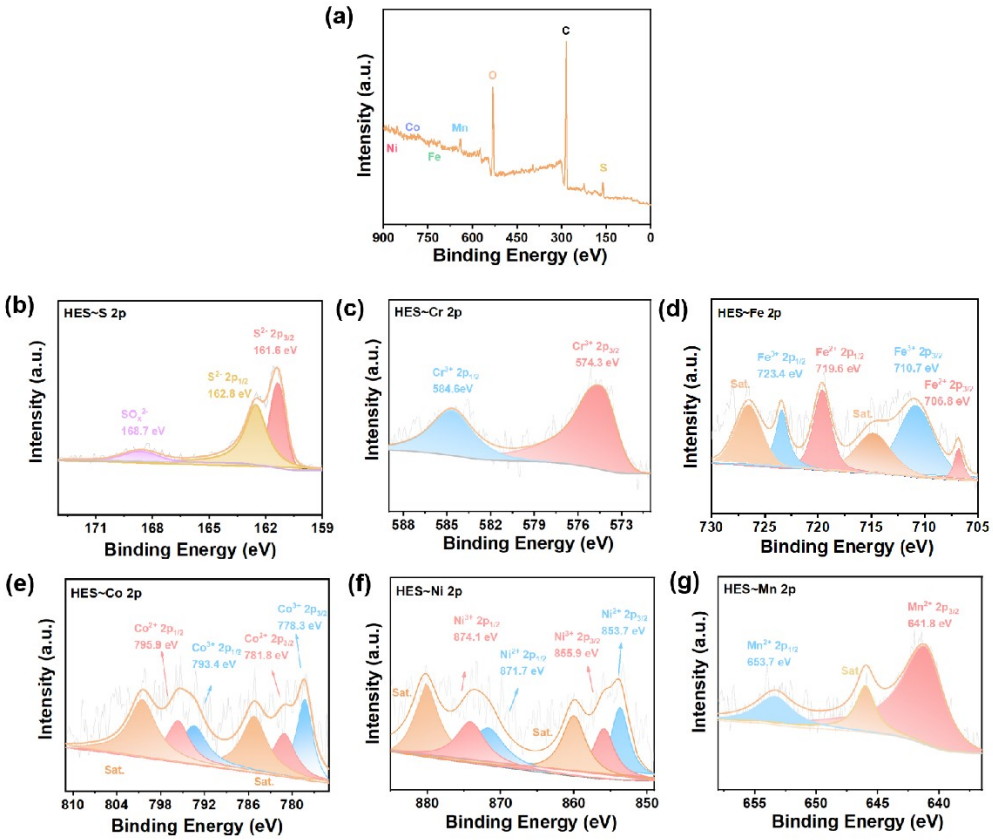

Fig. S8 XPS spectra of HES. (a) Full survey. High-resolution of (b) S 2p, (c)Cr 2p, (d) Fe 2p, (e) Co 2p, (f) Ni 2p, and (g) Mn 2p, respectively.

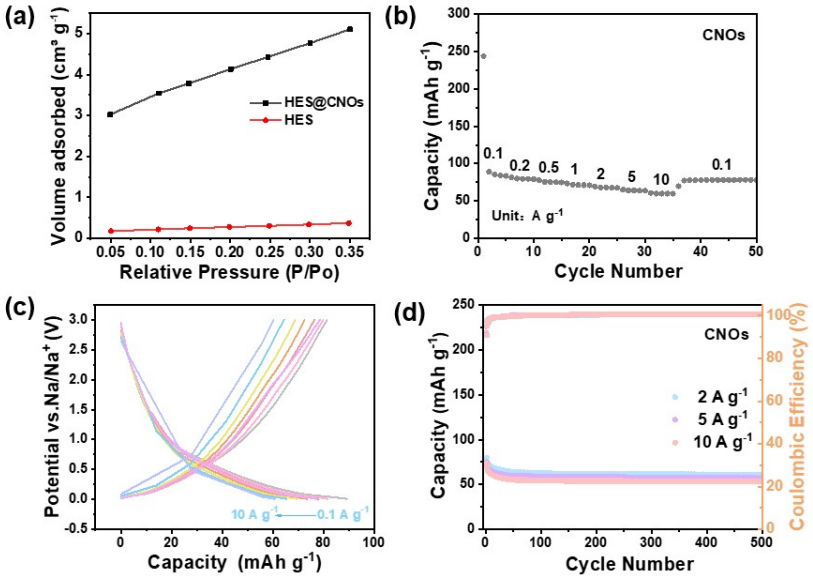

Fig. S9 (a) N_2 adsorption-desorption isotherms. (b) Rate performances of CNOs. (c) Corresponding charge/discharge curves at different current densities.

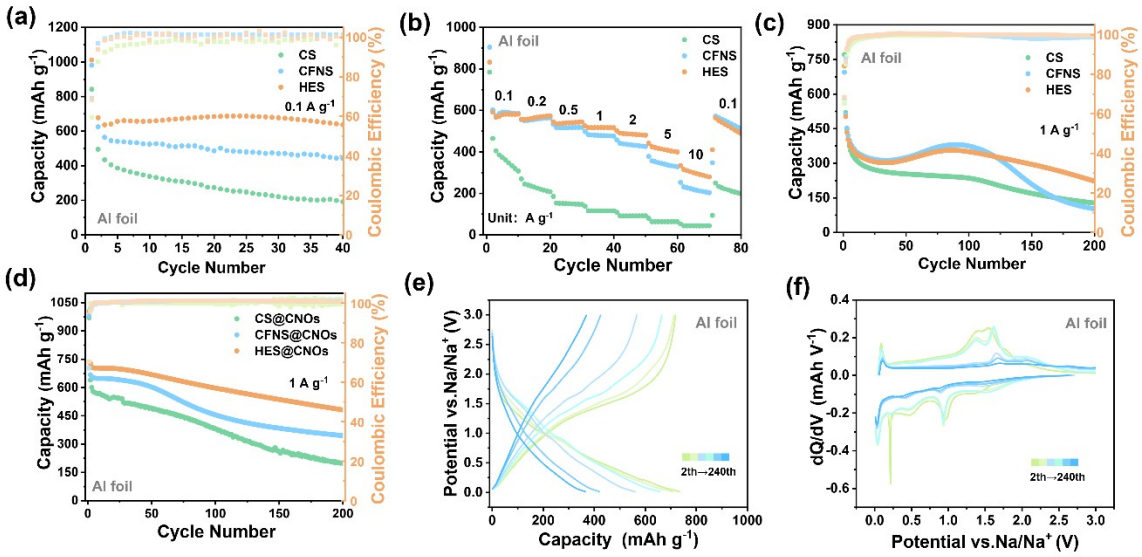

Fig. S10 (a) Cycling performances at 0.1 A g^{-1} and (b) Rate capabilities of CS, CFNS, and HES using Al foil. Comparison of cyclic performances at 1 A g^{-1} (c) CS, CFNS, and HES. (d) CS@CNOs, CFNS@CNOs, and HES@CNOs. (e) Discharge/charge profiles from 2nd to 240th cycles. (f) Corresponding dQ/dV curves.

Rate performance tests (Fig. 3b and Fig. S10b) further corroborated our findings, showing that HES@CNOs achieved discharge capacities of 761.4, 728.2, 707.3, 646.9, 600.5, 532.6, and 451.2 mAh g^{-1} at current densities of 0.1, 0.2, 0.5, 1, 2, 5, and 10 A g^{-1}, respectively. This performance significantly surpasses that of HES, which only reached 320.5 mAh g^{-1} at a current density of 10 A g^{-1}. However, the capacity of HES@CNOs declined to 481.3 mAh g^{-1} (Fig. 3c), corresponding to a capacity retention of 66.1% after 200 cycles at a current density of 1 A g^{-1}, while HES decreased to 222.5 mAh g^{-1} (Fig. S10c), reflecting a capacity retention ratio of 44.2%.

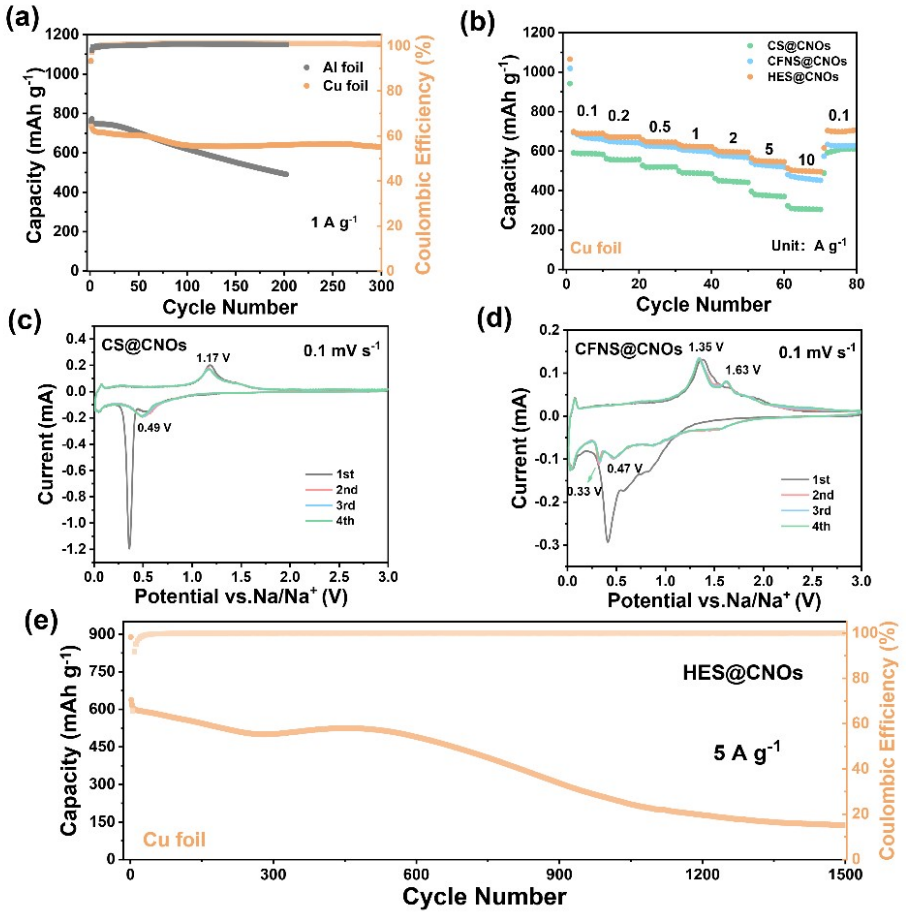

Fig. S11 (a) Comparison of electrochemical performances among Al foil and Cu foil at 1 A g^{-1}. (b) Rate capabilities of CS @CNOs, CFNS @CNOs, and HES @CNOs using Cu foil. CV curves of (c) CS @CNOs, and (d) CFNS @CNOs. (e) Cyclic performances of the electrode at 5 A g^{-1}.

HES@CNOs material coating on Cu foil exhibits specific capacities of 698.0, 671.1, 647.2, 624.2, 597.9, 557.1, and 502.6 mAh g^{-1} at current densities of 0.1, 0.2, 0.5, 1, 2, 5, and 10 A g^{-1}, respectively (Fig. S11b). When the current density returned to 0.1 A g^{-1}, HES@CNOs recovered a specific capacity of 703.8 mAh g^{-1}. The capacity variation between 0.1 and 10 A g^{-1} for HES@CNOs was calculated as 195.4 mAh g^{-1}, in contrast to a larger change of 280.7 mAh g^{-1} observed in CS@CNOs. This observation suggests that high-entropy materials provide enhanced sodium-ion diffusion across a range of charging and discharging rates. Fig. S11c and S11d present the CV tests of CS@CNOs and CFNS@CNOs, the two low-potential reversible peaks indicate sodium-ion intercalation and extraction within CNOs, which contribute additional capacity. Compared to HES@CNOs, CS@CNOs, with a simpler

composition, exhibits only two reaction peaks due to simpler redox behavior (Fig. S11c). However, the long-term cycling performance of HES@CNOs is far from ideal. As shown in Fig. S11e, the cycling performance of HES@CNOs on Cu foil at a high current density of 5 A g^{-1} reveals low reversible capacities of 136.5 mAh g^{-1} and a capacity retention ratio of only 21.4% after 1500 cycles.

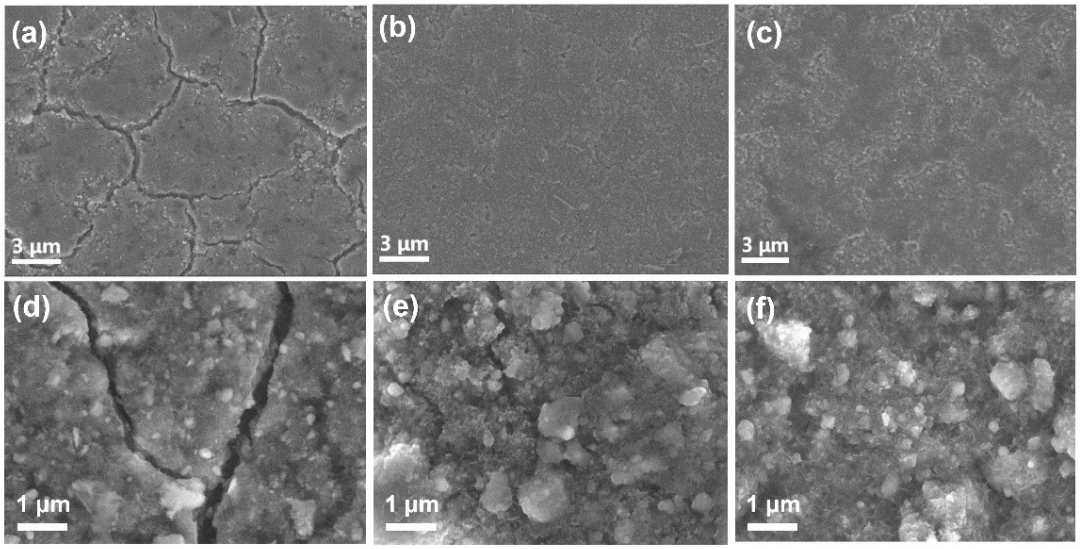

Fig. S12 Surface SEM images of the electrodes after 50 cycles at 1 A g^{-1} (a,d) CS@CNOs. (b,e) CFNS@CNOs. (c,f) HES@CNOs.

As illustrated in Fig. S12c and f, after 50 cycles at a current density of 1 A g^{-1}, the integrity of the HES@CNOs electrode remained largely intact, with minimal crack formation. In addition, the anode exhibited clear particles and no obvious shape. However, in Fig. S12a and d, significant crack propagation and fragmentation were observed in the CS@CNOs electrode, accompanied by thick SEI film, which can be attributed to continuous fracture, the electrolyte is depleted, leading to the formation of additional SEI.

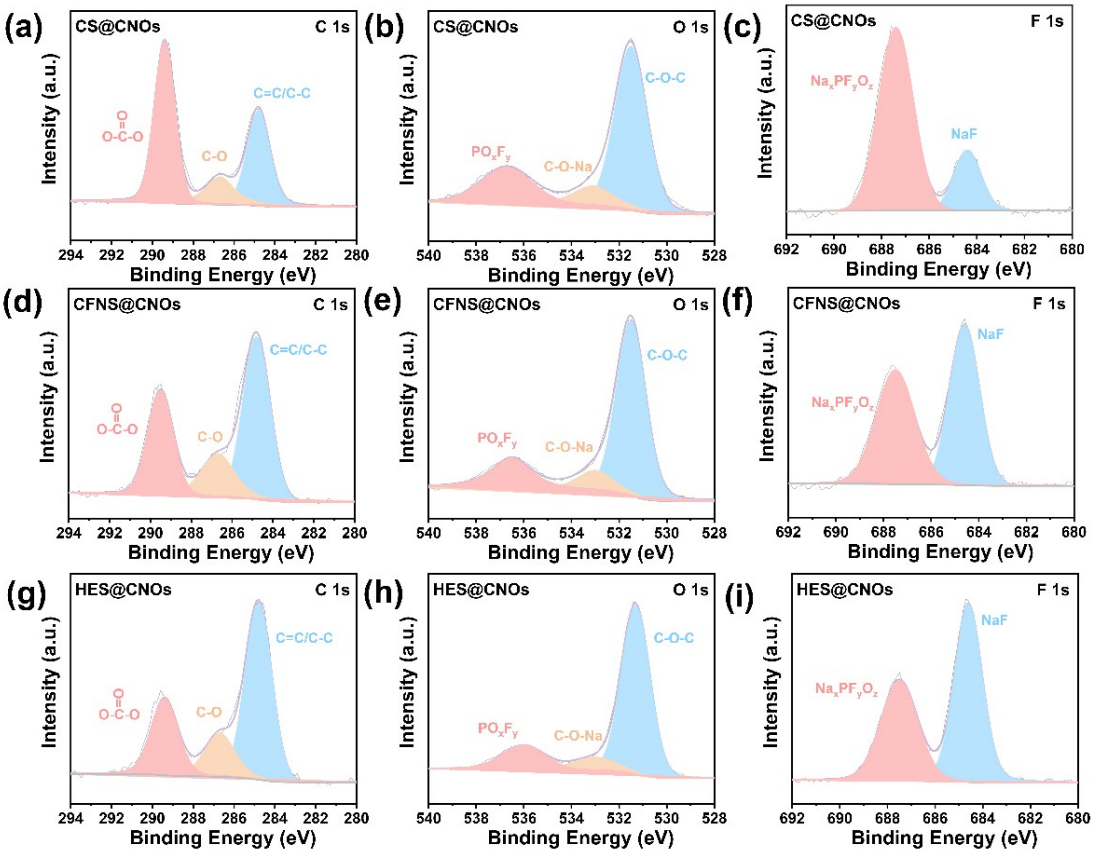

Fig. S13 HRXPS spectra of C 1s, O 1s, and F 1s for electrodes after 50 cycles. (a-c) CS@CNOs. (d-f) CFNS@CNOs. (g-i) HES@CNOs.

Compared to the other two electrodes, the C 1s spectrum shows that the SEI film derived from CS@CNOs is rich in O-(C=O)-O (Fig. S13a),[16] suggesting that organics species is predominant on SEI film surface. Meanwhile, as depicted in Fig. S13b, the SEI film generated by CS@CNOs, has more organic products, PF_yO_z, as well as in F 1s spectrum.[17] Different from this case, the SEI film obtained by HES@CNOs exhibits a prevailing peak of NaF on the surface (Fig. S13i). As for the SEI film derived from CFNS@CNOs, exhibits a similar composition of SEI film components compared to HES@CNOs (Fig. S13d-f). The high content of organics leads to an increase in internal resistance and inhibits the sodium ion transport.

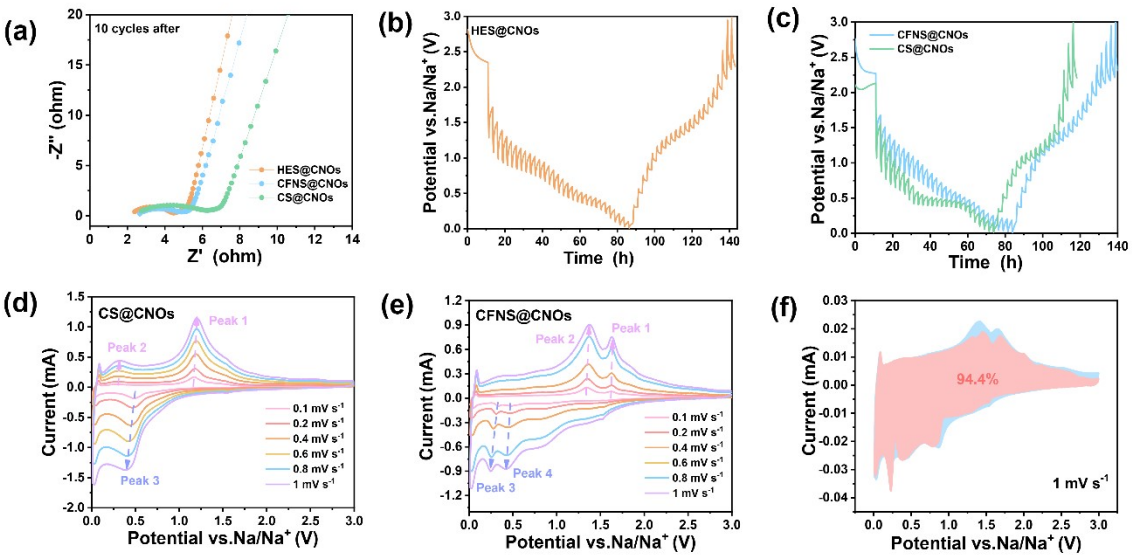

Fig. S14 (a) Nyquist plots of the electrodes after 10 cycles. GITT of electrodes over the first discharge and charge (b) HES@CNOs, (c) CS@CNOs and CFNS@CNOs. (d) CV curves at different scan rates of (d) CS@CNOs, (e) CFNS@CNOs. (f) Capacitive contribution of CV curves at 1.0 mV s^{-1} of HES@CNOs.

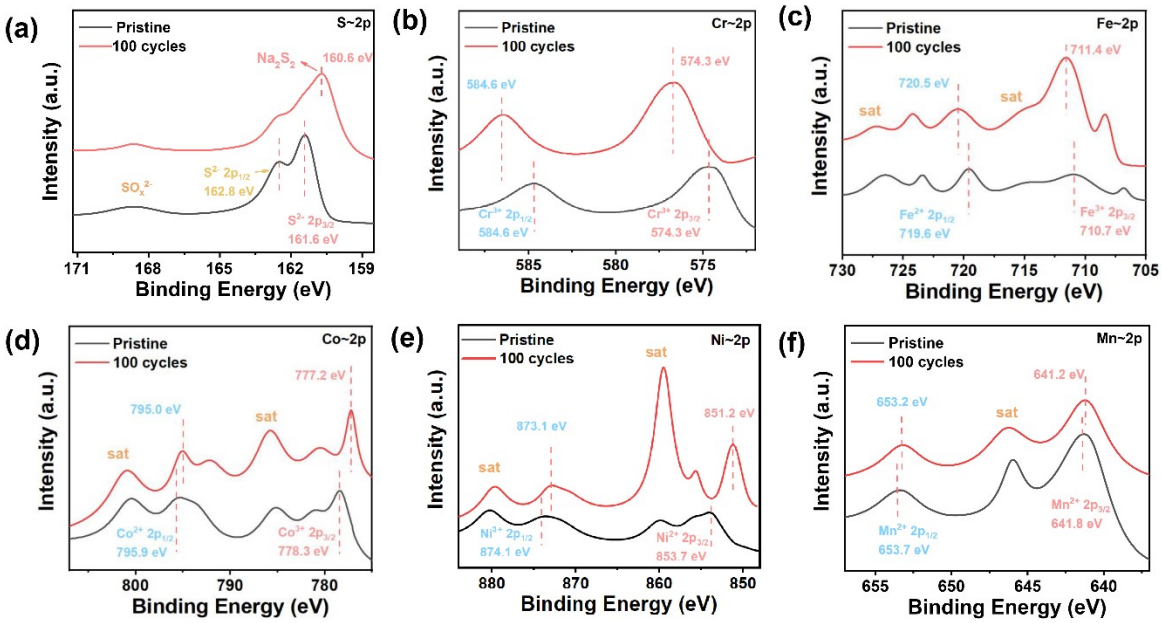

Fig. S15 Ex-situ XPS analysis of HES@CNOs electrodes before and after 100 cycles. Comparison of (a) S 2p, (b) Cr 2p, (c) Fe 2p, (d) Co 2p, (e) Ni 2p, and (f) Mn 2p high-resolution spectra.

In the dQ/dV curve (Fig. 4a), reduction peaks at 0.21, 0.47, and 0.97 V and oxidation peaks at 1.39 and 1.56 V gradually attenuate with increased cycling depth. New peaks emerge around 0.6 V, as well as at 1.52, 1.55, and 2.0 V, suggesting an evolving electrochemical profile. Similarly, as shown in Fig. 4b, the GCD curves exhibit a newly developed slope around 0.6 V and additional voltage plateau regions at 1.52, 1.55, and 2.0 V, indicating irreversible phase transformation in the material on Cu foil after extended cycling. To explore these transformations further, we conducted ex-situ XPS analysis on the active material extracted from electrodes after 100 and 300 cycles (Fig. S14). After 100 cycles, the spectra revealed peak shifts, confirming that conversion reactions are indeed irreversible.

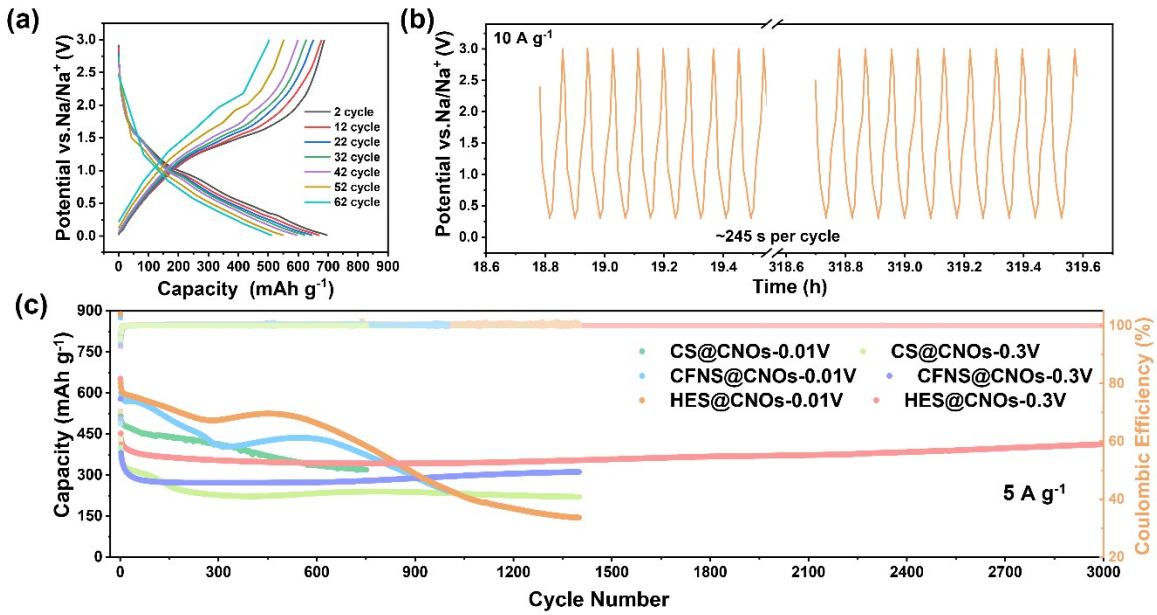

Fig. S16 (a) Charge/discharge profiles of HES@CNOs at various rates. (b) Time-voltage profiles of HES@CNOs electrode at 10 A g^{-1}. (c) Cyclic performances of the electrode at 5 A g^{-1} at different voltage windows.

In contrast to 0.3 V, rate cycling within 0.01-3 V led to changes in GCD curve shape, signaling copper reaction plateaus (Fig. S15a). When the voltage lower limit was elevated, electrodes manifested outstanding cycling performance. For instance, at 5 A g^{-1}, HES@CNOs maintained a capacity retention of 91.1% after 3000 cycles (Fig. S15c) and delivered a discharge capacity of 412.8 mAh g^{-1}. However, with a 0.01-3 V range, significant capacity decline was observed over time, in contrast to the consistent performance in the 0.3-3 V range, with minimal capacity decay (0.014% per cycle).

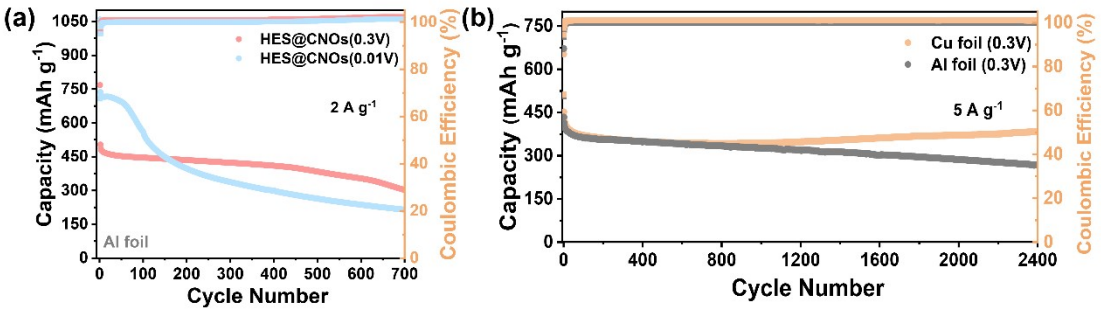

Fig. S17 (a) Cyclic performances of HES@CNOs (Al foil) at 2 A g^{-1} under different voltage windows. (b) Cyclabilities of HES@CNOs at 5 A g^{-1} with different current collectors.

Fig. S16b compares the capacity trends on both current collectors at 5 A g^{-1}, where the capacity reduction on Al foil indicates NaPS accumulation. In contrast, electrodes on Cu foil displayed a slight capacity increase, suggesting that copper reacts with Na_2S_x around the active material during cycling. This reaction retains some sulfur and generates new active material, Cu_xS.

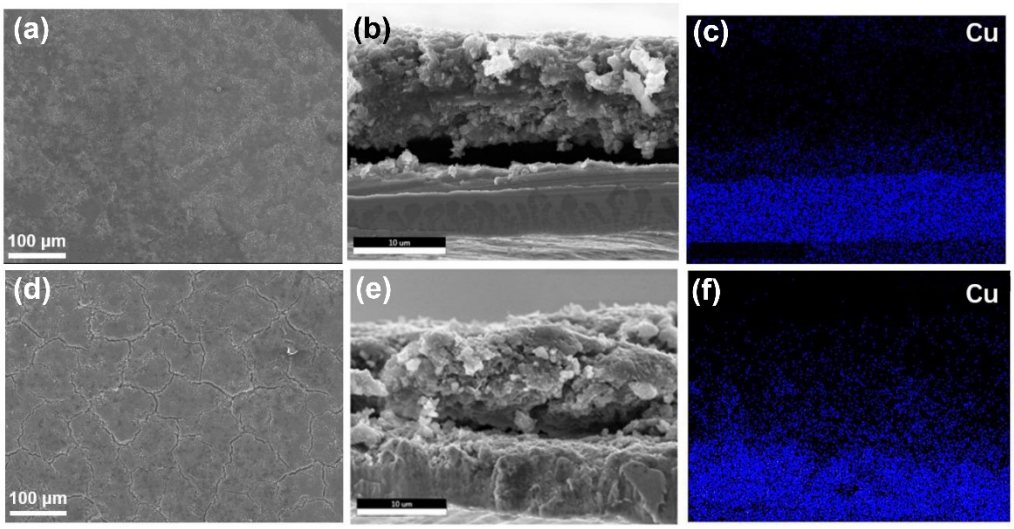

Fig. S18 Ex-situ SEM images for HES@CNOs after 200 cycles under different cut-off voltage (a-c) 0.01V and (d-f) 0.3V. (a,d) Surface images. (b,e) Cross-section images. (c,f) EDS mapping of Cu.

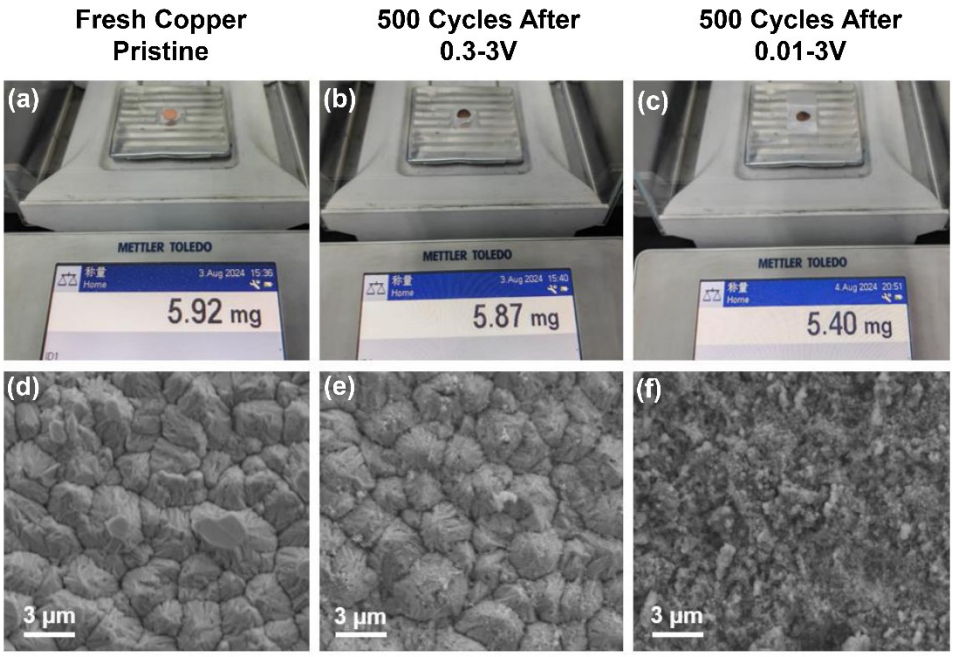

Fig. S19 Comparison of quality and surface images of original copper foil and cycled 500 times with different cut-off voltage. (a,d) Pristine. (b,e) 0.3-3V. (c,f) 0.01-3V.

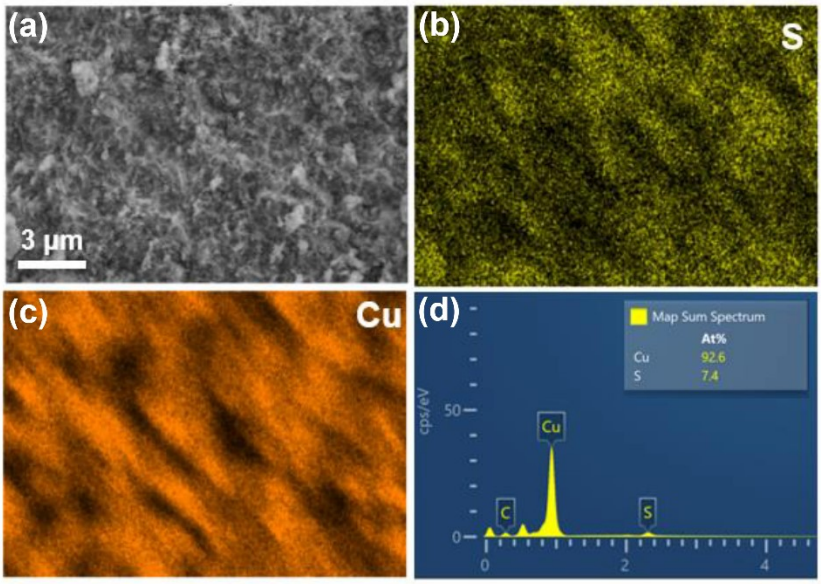

Fig. S20 (a) The surface scan image of the cycled current collector after 500 cycles in the voltage range of 0.01-3V. (b,c) Corresponding mapping. (d) Statistics of backscattered electron components.

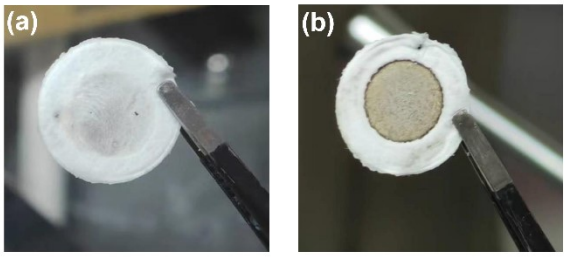

Fig. S21 Optical images of the separators after 200 cycles under different cut-off voltage (a) 0.3V and (b) 0.01V.

Ex-situ SEM analysis revealed substantial crack propagation on both the surface and cross-section of electrodes fully sodiated at 0.01 V (Fig. S17a,b and Fig. S17d,e), whereas at 0.3 V, this damage was minimized. Cross-sectional scans indicated copper's diffusion at active material interfaces, further supporting its involvement in side reactions. We also examined the mass and morphology of current collectors and separators after 500 cycles at 2 A g^{-1} under different voltage windows. As shown in Fig. S18a-c, the mass of the Cu foil after cycling in the 0.3-3 V window closely resembled that of the original foil, with minimal surface changes noted in SEM images

(Fig. S18d-f). In the 0.01-3 V range, however, a significant mass reduction and corroded nanocluster formation were observed. SEM mapping (Fig. S19) further revealed copper sulfide deposits on the Cu foil, confirming copper's involvement in side reactions. As shown in Fig. S20, optical images of the separators highlighted that reduced sodiation depth alleviates the NaPS shuttle effect.

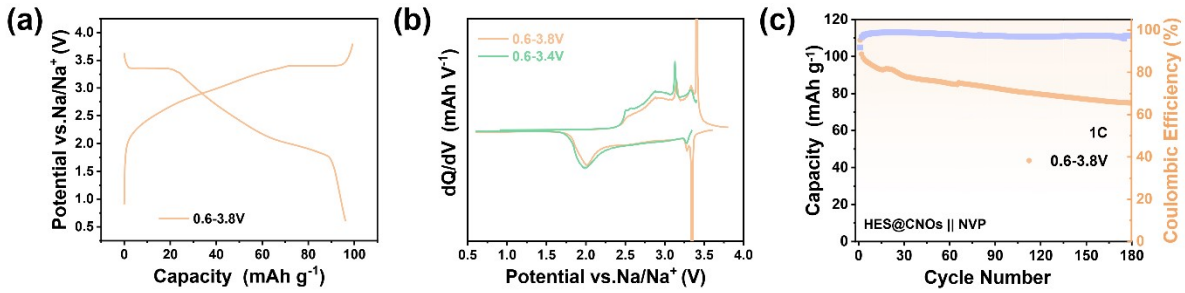

Fig. S22 (a) Discharge/charge profiles of full cell under 0.6-3.8V voltage window. (b) dQ/dV curves. (c) Cyclic performance of HES@CNOs||NVP at 1C rate.

In the full-cell tests conducted within a 0.6–3.8 V range (Fig. S21a), two distinct voltage plateau regions were noted, unlike the smoother profile observed in Fig. 7c. The dQ/dV curves (Fig. S21b) also reveal two prominent redox peaks between 3.4 V and 3.8 V, reflecting heightened redox activity in this range. In addition, when tested in the broader 0.6-3.8 V window, the full cell's capacity reduced to 74.7 mAh g^{-1} after 180 cycles, with a lower retention rate of 68.7% (Fig. S21c).

Table S1. Crystal-structural parameters of the CS from Rietveld refinement.

Atom	x	y	z	Occ	Site
Cr1	0.4853	0.5	0.2574	1	4i
Cr1	0.5	0.5	0.5	0.201	2a
Cr1	0	0	0.5	1	2d
S1	0.8356	0.5	0.3632	1	4i
S2	0.3235	0	0.3745	1	4i
	a=5.9713Å	**b=3.4420Å**	**c=11.3528Å**	**α=γ=90°**	**β=91.111°**

Table S2. Crystal-structural parameters of the CFNS from Rietveld refinement.

Atom	x	y	z	Occ	Site
Ni1	0.5	0	0.5	0.262	2b
Fe1	0.5	0	0.5	0.262	2b
Cr	0	0.5	0.5	1	2c
Fe2	0.51605	0	0.25862	0.25	4i
Ni2	0.51605	0	0.25862	0.25	4i
S1	0.88508	0	0.37416	1	4i
S2	0.337	0.5	0.38613	1	4i
	a=5.92119Å	**b=3.42192Å**	**c=11.0960Å**	**α=γ=90°**	**β=91.0369°**

Table S3. Crystal-structural parameters of the HES from Rietveld refinement.

Atom	x	y	z	Occ	Site
Ni1	0.51140	1	0.74300	0.286	4i
Fe1	0.51140	1	0.74300	0.370	4i
Cr	1	0.5	0.5	1	2c
Co1	0.51140	1	0.74300	0.310	4i
Mn1	0.5	0	0.5	0.2	2b
S1	0.66890	0.5	0.62710	1	4i
S2	0.16140	1	0.63600	1	4i
	a=5.93590Å	**b=3.42530Å**	**c=11.5800Å**	**α=γ=90°**	**β=90.8900°**

Table S4. Electrochemical performance comparison of various metal sulfide anode materials for sodium-ion batteries.

Sample	Current Density ($A\ g^{-1}$)	Reversible Capacity ($mAh\ g^{-1}$)	Cycle Number	References
CC-ZnS/CNT	5	314	500	1
P-CoS_x/N, S-PC	2	408	1000	2
CoS_2/NC	2	590	900	3
MoS_2/Sb_2S_3@C	5	411.5	650	4
NiS@NCNT	1	290	500	5
FeCo-NiS	2	514	600	6
CoS/Cu_2S@C-NC	2	435.3	1000	7
ZCTS	5	516	2000	8
Co_3S_4@NiS_2/C	10	143.2	2000	9
FeS@C	10	288	3000	10
	2	**436.7**	**3000**	
HES@CNOs	**5**	**412.8**	**3000**	**This work**
	10	**352.2**	**3800**	

Table S5. Rate performance comparison of various metal sulfide anode materials for sodium-ion batteries.

Sample	Current Density ($A\ g^{-1}$)	Capacity ($mAh\ g^{-1}$)	References
CC-ZnS/CNT	1,2,5	446, 413, 346	1
P-CoS_x/N,S-PC	1,2,5	418, 402, 370	2
(FeCoNiCuRu)S_2	1,2,5,10	500, 486, 467, 458	11
CoS_2/NiS_2	1,2,5	444, 373, 275	12
MoS_2/SnS/rGO	1,2,5,10	425.4, 399.5, 325.2, 239.0	13
Bi_2S_3/MoS_2	1,2,5	350, 335, 330	14
$Cu_4MnFeSnGeS_8$	1,2,5,10	533.9, 504.1, 477.4, 459.2	15
HES@CNOs(0.3-3V)	**1,2,5,10**	**473.9, 457.6, 437.3, 416.6**	**This work**
HES@CNOs(0.01-3V)	**1,2,5,10**	**633.4, 608.0, 565.0, 512.8**	**This work**

Table S6. Comparison of R_{ct} before and after cycling.

Sample	R_{ct} (Pristine)	R_{ct} (10 cycles after)
CS@CNOs	17.33 Ω	3.79 Ω
CFNS@CNOs	8.18 Ω	2.55 Ω
HES@CNOs	2.06 Ω	1.96 Ω

A comparative analysis of the fitting results (Fig. 3e, Fig. S13a, and Table S6) reveals that HES@CNOs exhibited a lower charge transfer resistance (R_{ct}), which decreased to 1.96 Ω after 10 cycles. The resistance reduction is attributed to the improved conductivity of electrons and ions in the activated electrode.

Table S7. Fitting results of electrical conductivity for SIBs from EIS.

Sample	σ_e ($\times 10^{-3}$ S m^{-1})
CS@CNOs	15.2
CFNS@CNOs	28.2
HES@CNOs	45.3

By measuring the area S and thickness l of each electrode and calculating the conductivity σ_e by using the formula $\sigma_e = l/(RS)$, the results shown in Table S7 indicate that HES@CNOs has the highest conductivity (4.53×10^{-2} S m^{-1}).

Table S8. Sodium ion average diffusion coefficient at charge/discharge state of CS@CNOs, CFNS@CNOs, and HES@CNOs electrodes, respectively.

Sample	$Na_{Dis.}$ (cm^2 s^{-1})	$Na_{Cha.}$ (cm^2 s^{-1})
CS@CNOs	7.76×10^{-11}	1.61×10^{-10}
CFNS@CNOs	1.18×10^{-10}	2.70×10^{-10}
HES@CNOs	1.67×10^{-10}	3.07×10^{-10}

Table S9. The energy density of the full cell.

Voltage Window (V)	Energy Density (Wh kg^{-1})
0.6-3.4	246.6
0.6-3.8	275.8

The energy density (E, Wh kg^{-1}) was calculated by the following formula:

$$E = \int Q\, dV = \int_{t_1}^{t_2} IV_{(t)} dt$$

where t_1 and t_2 are the discharge start and end time (s), respectively, V indicates the working potential (V) and I presents the constant current (A).

It is obvious that narrowing the voltage window would slightly decrease the energy density.

References

[1] T. Hou, B. Liu, X. Sun, A. Fan, Z. Xu, S. Cai, C. Zheng, G. Yu, A. Tricoli, *ACS Nano.* **2021**, *15*, 6735-6746.

[2] X. Yin, Y. Ren, L. Wu, Z. Zhang, C. Du, J. Wang, G. Yin, H. Huo, *J. Energy Chem.* **2022**, *71*, 210-217.

[3] L. Chen, N. Luo, S. Huang, Y. Li, M. Wei, *Chem. Commun.* **2020**, *56*, 3951-3954.

[4] D. Wang, L. Cao, D. Luo, R. Gao, H. Li, D. Wang, G. Sun, Z. Zhao, N. Li, Y. Zhang, *Nano Energy.* **2021**, *87*, 106185.

[5] S. Fan, S. Huang, Y. Chen, Y. Shang, Y. Wang, D. Kong, M. E. Pam, L. Shi, Y. W. Lim, Y. Shi, *Energy Storage Mater.* **2019**, *23*, 17-24.

[6] J. Liu, C. Lou, J. Fu, X. Sun, J. Hou, J. Ma, Y. Chen, X. Gao, L. Xu, Q. Wei, *J. Energy Chem.* **2022**, *70*, 604-613.

[7] X. Huang, K. Tao, T. Han, J. Li, H. Zhang, C. Hu, J. Niu, J. Liu, *Small.* **2023**, *19*, 2302706.

[8] W. Li, C. Yu, S. Huang, C. Zhang, B. Chen, X. Wang, H. Y. Yang, D. Yan, Y. Bai, *Adv. Mater.* **2024**, *36*, 2305957.

[9] X. Huang, R. Wang, L. Wu, H. Zhang, J. Liu, *Small.* **2023**, *19*, 2304165.

[10] D. Yang, W. Chen, X. Zhang, L. Mi, C. Liu, L. Chen, X. Guan, Y. Cao, C. Shen, *J. Mater. Chem. A.* **2019**, *7*, 19709-19718.

[11] W. Cheng, J. Liu, J. Hu, W. Peng, G. Niu, J. Li, Y. Cheng, X. Feng, L. Fang, M. S. Wang, *Small.* **2023**, *19*, 2301915.

[12] J. Wang, X. Yue, X. Cao, Z. Liu, A. M. Patil, J. Wang, X. Hao, A. Abudula, G. Guan, *Chem. Eng. J.* **2022**, *431*, 134091.

[13] Y. Yan, P.-Q. Li, Z.-Y. Gu, W. Liu, J.-M. Cao, X.-L. Wu, *Chem. Eng. J.* **2022**, *432*, 134195.

[14] L. Cao, X. Liang, X. Ou, X. Yang, Y. Li, C. Yang, Z. Lin, M. Liu, *Adv. Funct. Mater.* **2020**, *30*, 1910732.

[15] J. Zhao, Y. Zhang, X. Chen, G. Sun, X. Yang, Y. Zeng, R. Tian, F. Du, *Adv. Funct. Mater.* **2022**, *32*, 2206531.

[16] K. Li, J. Zhang, D. Lin, D.-W. Wang, B. Li, W. Lv, S. Sun, Y.-B. He, F. Kang, Q.-H. Yang, *Nat. Commun.* **2019**, 10, 725.

[17] X. Xu, Y. Liu, X. Luo, G. Ma, F. Tian, Y. Li, D. Zhang, J. Yang, *Energy Storage Mater.* **2021**, 40, 189-196.